Refraction limit of miniaturized optical systems: a ball-lens example

Myun-Sik Kim,[1,6,*] Toralf Scharf,[1] Stefan Mühlig,[2] Martin Fruhnert,[3] Carsten Rockstuhl,[3,4] Roland Bitterli,[5] Wilfried Noell,[6] Reinhard Voelkel,[6] and Hans Peter Herzig[1]

[1]*Optics & Photonics Technology Laboratory, Ecole Polytechnique Fédérale de Lausanne (EPFL), Neuchâtel, CH-2000, Switzerland*
[2]*Institute of Condensed Matter Theory and Solid State Optics, Abbe Center of Photonics, Friedrich-Schiller-Universität Jena, 07743 Jena, Germany*
[3]*Institute of Theoretical Solid State Physics, Karlsruhe Institute of Technology, 76131 Karlsruhe, Germany*
[4]*Institute of Nanotechnology, Karlsruhe Institute of Technology, 76021 Karlsruhe, Germany*
[5]*Instant-Lab, Ecole Polytechnique Fédérale de Lausanne (EPFL), Neuchâtel, CH-2000, Switzerland*
[6]*SUSS MicroOptics SA, Rouges-Terres 61, Hauterive, CH 2068, Switzerland*
[*]*myun-sik.kim@epfl.ch*

Abstract: We study experimentally and theoretically the electromagnetic field in amplitude and phase behind ball-lenses across a wide range of diameters, ranging from a millimeter scale down to a micrometer. Based on the observation, we study the transition between the refraction and diffraction regime. The former regime is dominated by observables for which it is sufficient to use a ray-optical picture for an explanation, e.g., a cusp catastrophe and caustics. A wave-optical picture, i.e. Mie theory, is required to explain the features, e.g., photonic nanojets, in the latter regime. The vanishing of the cusp catastrophe and the emergence of the photonic nanojet is here understood as the refraction limit. Three different criteria are used to identify the limit: focal length, spot size, and amount of cross-polarization generated in the scattering process. We identify at a wavelength of 642 nm and while considering ordinary glass as the ball-lens material, a diameter of approximately 10 μm as the refraction limit. With our study, we shed new light on the means necessary to describe micro-optical system. This is useful when designing optical devices for imaging or illumination.

©2016 Optical Society of America

OCIS codes: (260.0260) Physical optics; (290.4020) Mie theory; (260.1960) Diffraction theory.

References and links

1. M. V. Berry, "Rays, wavefronts and phase: a picture book of cusps," Proc. Huygens Symp., ed. H. Blok, H.A. Ferwerda, and H.K. Kuiken, *Huygens' Principle 1690–1990: Theory and Applications* (Elsevier Science Publishers B.V., 1992).
2. T. Pearcey, "The structure of an electromagnetic field in the neighbourhood of a cusp of a caustic," Philos. Mag. **37**(268), 311–317 (1946).
3. M. Born and E. Wolf, *Principles of Optics*, 7th ed. (Cambridge University, 1999).
4. J. J. Stamnes, *Waves in Focal Regions* (Adam Hilger, 1986).
5. F. Träger, *Handbook of Lasers and Optics* (Springer, 2007).
6. M. Riedl, *Optical Design Fundamentals for Infrared Systems* (SPIE, 2001), 2nd ed.
7. R. P. Ratowsky, L. Yang, R. J. Deri, J. S. Kallman, and G. Trott, "Ball lens reflections by direct solution of Maxwell's equations," Opt. Lett. **20**(20), 2048–2050 (1995).
8. R. G. Wilson, "Ball-lens coupling efficiency for laser-diode to single-mode fiber: comparison of independent studies by distinct methods," Appl. Opt. **37**(15), 3201–3205 (1998).
9. H. Guo, Y. Han, X. Weng, Y. Zhao, G. Sui, Y. Wang, and S. Zhuang, "Near-field focusing of the dielectric microsphere with wavelength scale radius," Opt. Express **21**(2), 2434–2443 (2013).
10. Z. Chen, A. Taflove, and V. Backman, "Photonic nanojet enhancement of backscattering of light by nanoparticles: a potential novel visible-light ultramicroscopy technique," Opt. Express **12**(7), 1214–1220 (2004).
11. A. Heifetz, S.-C. Kong, A. V. Sahakian, A. Taflove, and V. Backman, "Photonic nanojets," J. Comput. Theor. Nanosci. **6**(9), 1979–1992 (2009).

#254854 Received 1 Dec 2015; revised 7 Mar 2016; accepted 8 Mar 2016; published 22 Mar 2016
© 2016 OSA

12. Z. Wang, W. Guo, L. Li, B. Luk'yanchuk, A. Khan, Z. Liu, Z. Chen, and M. Hong, "Optical virtual imaging at 50 nm lateral resolution with a white-light nanoscope," Nat. Commun. **2**, 218 (2011).
13. M. X. Wu, B. J. Huang, R. Chen, Y. Yang, J. F. Wu, R. Ji, X. D. Chen, and M. H. Hong, "Modulation of photonic nanojets generated by microspheres decorated with concentric rings," Opt. Express **23**(15), 20096–20103 (2015).
14. K. Youngworth and T. Brown, "Focusing of high numerical aperture cylindrical-vector beams," Opt. Express **7**(2), 77–87 (2000).
15. K. Bahlmann and S. W. Hell, "Depolarization by high aperture focusing," Appl. Phys. Lett. **77**(5), 612–614 (2000).
16. B. Sick, B. Hecht, U. P. Wild, and L. Novotny, "Probing confined fields with single molecules and vice versa," J. Microsc. **202**(2), 365–373 (2001).
17. M.-S. Kim, T. Scharf, and H. P. Herzig, "Small-size microlens characterization by multiwavelength high-resolution interference microscopy," Opt. Express **18**(14), 14319–14329 (2010).
18. M.-S. Kim, T. Scharf, S. Mühlig, C. Rockstuhl, and H. P. Herzig, "Engineering photonic nanojets," Opt. Express **19**(11), 10206–10220 (2011).
19. M.-S. Kim, T. Scharf, S. Mühlig, C. Rockstuhl, and H. P. Herzig, "Gouy phase anomaly in photonic nanojets," Appl. Phys. Lett. **98**(19), 191114 (2011).
20. Y. Li and E. Wolf, "Three-dimensional intensity distribution near the focus in systems of different Fresnel numbers," J. Opt. Soc. Am. A **1**(8), 801–808 (1984).
21. U. Vokinger, R. Dändliker, P. Blattner, and H. P. Herzig, "Unconventional treatment of focal shift," Opt. Commun. **157**(1-6), 218–224 (1998).

1. Introduction

When light interacts with matter, it typically exhibits ray and wave optical characteristics at the same time. Which of the both characteristics dominates, implying different effects that occur predominantly, may vary depending on the characteristic dimension of the object with respect to the wavelength of light. Furthermore, the character of light waves evolves from a scalar to a vector under a tighter confinement. A good example for the coexistence of ray and wave characteristics can be found in an aberrated focus. When a monochromatic light wave propagates through an imperfect focusing system, a cusp catastrophe occurs, in which caustics and a cusp are a manifestation of catastrophe theory in optics [1]. Intuitive explanations of this phenomenon rely on geometrical optics. Such theory is usually applicable in the short-wave limit, i.e., when all geometrical features are much larger than the wavelength. More precise descriptions require considering the wave nature of light. For instance, the fold and cusp catastrophes explain the disappearance of the caustic singularity by demonstrating that it is an artifact of the geometrical optics limit [1]. In theory, Pearcey has found an exact solution for waves near a cusp in 1946 [2]. Experimentally, the cusp catastrophe can be observed with a lens possessing a spherical aberration. Numerous studies have been carried out and textbook examples for waves near the focus of an imperfect lens are available [3, 4]. However, an experimental study of the cusp catastrophe beyond the short-wave limit has not been reported. Here, we study the cusp catastrophe beyond the conventional short-wave limit by decreasing the characteristic dimension of the object that causes it. This allows us to distinguish optical regimes, where either wave-optical or ray-optical features dominate the observables.

In this study, we employ one of the most natural examples for an imperfect lens that can produce the cusp catastrophe: a dielectric sphere. Dielectric spheres are generally described by a double-convex-type thick lens, commonly called a ball-lens [5]. Note that its spherical surface profile intrinsically leads to a strong spherical aberration. As mentioned before, the cusp catastrophe can be caused by such an aberrated focus. Relatively large ball-lenses have been intensively studied for optical-fiber communication systems [6–8]. Its characteristics are well studied by geometric optics under paraxial approximation [5]. The origins of the numerical aperture (NA) and the spherical aberration of the wavelength-scale ball-lens have been reported using rigorous theory and numerical simulations [9]. Interestingly, when the size of the sphere becomes comparable to the illuminating wavelength leading to the scattering domain, a specific light confinement occurs, named *photonic nanojet* [10, 11]. Such a phenomenon is proven to support super-resolution effects, for instance, super-resolution

#254854 Received 1 Dec 2015; revised 7 Mar 2016; accepted 8 Mar 2016; published 22 Mar 2016
© 2016 OSA

imaging capability of nanoscopes [12] and can be modulated by nano-structures on a sphere [13].

We are particularly interested in the transition region between a refractive focusing effect of the ball-lens and a tighter confinement of the photonic nanojet effect. The regimes are distinguished in a sense that both the focal length and width of the focal spot depend on the diameter of the ball-lens in the refraction domain, whereas they are size-independent in the diffraction domain. Then, the dominant mechanism of the light confinement shifts from refraction that is modeled by geometrical optics to the scattering regime which is described rigorously by Mie theory. Meanwhile, the short-wave approximation gradually becomes invalid as this transition occurs. At the point of transition, the cusp catastrophe, which is the canonical proof of refraction in an aberrated focus, vanishes and the form of the light confinement mimics an aplanatic focus without aberrations. Furthermore, the strong confinement of the photonic nanojet pushes the vector nature of light more noticeable, which can be proven by a depolarization effect of a high NA focus system [14–16]. This transitional point is understood here as the refraction limit.

2. Experiment and simulation details

Experiments are carried out using a high-resolution interference microscope (HRIM) [17, 18] to measure the 3D amplitude and phase distributions near a focus, which is a cusp (i.e., the peak confinement). We use a 100X/NA0.9 objective (Leica Microsystems, HC PL FLUOTAR) which assures the highest resolution of microscopy systems in air. The HRIM is equipped with a laser diode light source emitting at 642 nm wavelength (CrystaLaser, DL640-050-3). More details of the experimental setup are reported elsewhere [17, 18]. Dielectric spheres of diameters from 2 mm down to 1 μm are considered. Due to a broad range of the sphere size, spheres made from an identical material were not available. However, materials were chosen that possess only a marginal difference in optical properties. Microspheres made from polystyrene (n = 1.59), borosilicate glass (n = 1.56), N-BK7 (n = 1.52) and soda lime glass (n = 1.51) were considered. The sphere sizes for polystyrene, borosilicate and soda lime glass are 1 μm - 100 μm, 1 μm - 22 μm, and 100 μm - 400 μm, respectively, purchased from Duke Scientific Inc. For large-size spheres (diameter from 0.5 mm to 2 mm), N-BK7 spheres are purchased from Edmund Optics. For experimental convenience, spheres are dispersedly deposited on a glass substrate (Carl Roth, Borosilicate coverslip with thickness of 150 μm). For the experiment, we choose a single sphere, which is well isolated from other spheres. In experiments, a plane wave propagating along the positive z-direction and polarized in the x–direction illuminates the spheres from the substrate side. Surrounding medium of the sphere is air. Since the planar surface of the glass substrate does not affect in good approximation the spatial distribution of the plane wave but only changes its amplitude by imposing a Fresnel reflection coefficient, we consider in the simulations a plane wave as illumination for the sphere without substrate. Depending on the sphere size, numerical simulations using either a ray tracing (a commercial tool, FRED) or a full wave solution (i.e., Mie theory, see details in [18, 19]) are used to compare measurements to theoretical predictions. In brief, Mie simulations are carried out taking into account the optical imaging system using scalar propagation techniques in spatial frequency space. We calculate at first the electric field $E_x(x,y,z,\omega)$ and $E_y(x,y,z,\omega)$ with Mie theory in the x-y-plane at a distance z far away from the sphere, for instance, z = 10 μm for 1-μm sphere. After Fourier transforming the field to the spatial frequency space [$E_x(k_x,k_y,z$ = 10μm) and $E_y(k_x,k_y,z$ = 10μm)], we suppress all contributions of spatial frequencies (k_x and k_y) whose absolute value is larger than the numerical aperture of the observing objective divided by the incident wavelength. This mimics the behavior of the objective in the experiments. This modified electric field components are propagated to the slice of interest in z-direction by means of free space propagation.

#254854 Received 1 Dec 2015; revised 7 Mar 2016; accepted 8 Mar 2016; published 22 Mar 2016
© 2016 OSA

3. Geometrical representation of the ball-lens: ray optics

We start our discussion with a ray-optical representation of the ball-lens problem visualized in Fig. 1(a). For simplicity, the position of the peak intensity on the optical axis is defined as the focal point. The principal planes are set at the center of the sphere. Under paraxial approximation, an effective focal length (*EFL*) and a back focal length (*BFL*) can be found as [5, 9]:

$$EFL = \frac{nR}{2(n-1)}, \tag{1}$$

$$BFL = EFL - R, \tag{2}$$

where n is the refractive index of the sphere and R the radius of the sphere. The *EFL* [Eq. (1)] is measured from the center of the ball lens, and the *BFL* [Eq. (2)] from its rear surface. The back focal length will be examined as a criterion for the refraction limit in Section 5.1. Figure 1(b) shows a ray diagram emerging from the rear surface of a glass ball-lens (n = 1.5) calculated by FRED. One can see a typical cusp catastrophe represented by caustics forming a cusp in a triangular shape.

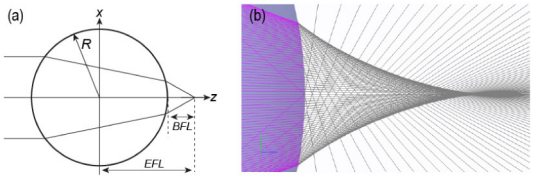

Fig. 1. (a) Geometrical optical parameters of a ball-lens, where *EFL* is effective focal length, *BFL* back focal length, and *R* the radius of the sphere. (b) FRED ray diagram emerging from the rear surface of a glass ball-lens.

4. Cusp catastrophe

4.1 Coexistence of the ray and wave nature of light: geometrical wavefront

An exemplary measurement of amplitude and phase distributions of the cusp catastrophe is shown in Fig. 2, using a 200-µm soda lime glass ball-lens. In the lower half of Figs. 2(a) and 2(b), we can observe the typical footprint of the spherical aberration in both intensity and phase measurements.

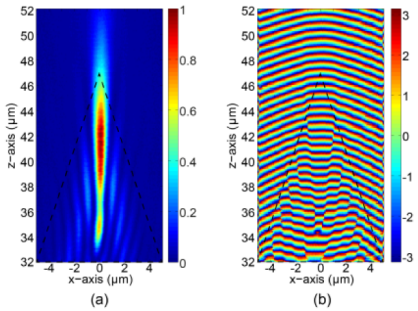

Fig. 2. (a) Measured *x*-*z* intensity and (b) phase distributions near the focus. The cusp catastrophe is created by a 200-µm soda lime glass ball-lens. Intensity is normalized and the surface of the ball-lens is on z = 0 plane

The short-wave approximation starts to be invalid and the wave nature of light becomes stronger. Consequently, the caustic lines are not prominent anymore. However, the vague footprint of the triangular area (see the dashed triangle in Fig. 2), where two caustics meet and

#254854 Received 1 Dec 2015; revised 7 Mar 2016; accepted 8 Mar 2016; published 22 Mar 2016
© 2016 OSA

form a cusp, is still observable. Outside this triangular area, the geometrical wavefronts appear, which are the iso-phase curves perpendicular to the single rays [1]. They demonstrate the coexistence of the ray and wave natures of light. In catastrophe theory [1], these geometrical wavefronts are singular at caustics and have a parabolic shape in the far field. In Fig. 2(b), such singularities of the geometric wavefront can be found near the triangular area and the parabolic shape in the area of $z > 47$ μm.

The spherical aberration broadens the size of the focal spot along both the axial (z) and lateral (x and y) directions and causes an asymmetry in the axial field distribution. A typical phase singularity of the focal spot is also found near the focal plane (i.e., near the cusp) due to the destructive interference that causes amplitude zeros around the focal spot. The strong amplitude of the side lobes in the out-of-focus planes, z from 0 to 10 μm, leads to additional wavefront dislocations, which are predictable by Pearcey's diffraction patterns [1, 2]. In the measurement of Fig. 2, the focal point is found approximately 42 μm away from the rear surface of the ball-lens, while Eq. (2) predicts 48 μm. This discrepancy can be explained by diffraction effects and spherical aberrations, as they are well-known causes to shift the focal point toward the lens [20, 21].

4.2 The vanishing of the cusp catastrophe

To visualize the evolution of the cusp catastrophe, we take a close look at the transient region between the refractive focusing of the ball-lens and the photonic nanojet. Spheres of diameter from 10 μm to 30 μm are considered. Figure 3 shows the x-z intensity distributions near the focus of those spheres.

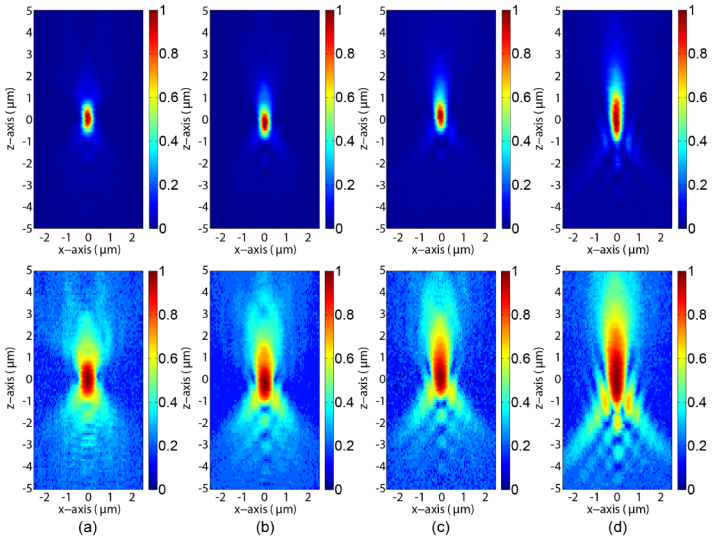

Fig. 3. The x-z intensity distributions of the focal spots created by the polystyrene ball-lens of (a) 10-μm, (b) 15-μm, (c) 20-μm, and (d) 30-μm diameters: (upper row) linear-scale intensity and (lower row) logarithmic-scale intensity maps. For easy comparison, the spot is aligned in the middle of each image and intensities are all normalized.

Logarithmic-scale intensity maps, shown in the lower row, emphasize the low intensity region compared to the maps in the upper row. The transition from the refractive focal spots shown in Figs. 3(b)-3(d) to the photonic nanojet in Fig. 3(a) is clearly observed as the disappearance of the triangular footprint of caustics. This means that for diameter D ≤ 10 μm the cusp catastrophe vanishes. The measurements of the smaller spheres are not shown in this section, but they show similar intensity distributions to that of Fig. 3(a). In this region, the

#254854 Received 1 Dec 2015; revised 7 Mar 2016; accepted 8 Mar 2016; published 22 Mar 2016
© 2016 OSA

intensity distribution remains symmetric with respect to the focal plane and no traces of the caustics are observed.

5. Criteria for the refraction limit

In the previous section, we discussed the particular features of the cusp catastrophe and its vanishing upon emergence of the photonic nanojet. In this section, we focus on identifying criteria for the refraction limit of the ball-lens by investigating focal length, spot size, and amount of cross-polarization.

5.1 Focal length

Figure 4 plots the extracted *BFL* from the measurements together with results of Eq. (2), which are represented by lines. For a more in-depth comparison, a commercial ray-tracing tool FRED is applied to calculate the focal length and the spot size for the corresponding ball-lens materials, and results are plotted as black open squares. Experimental results of the *BFL* show a good agreement with Eq. (2) for the ball-lens sizes down to 100 μm. For ball-lenses of D < 100 μm, the discrepancy between experiments and ray-optic calculations starts to be more notable. For smaller diameters (D ≤ 20 μm), the Mie simulation leads to a better agreement with experiments, which is plotted as red asterisks. For D ≤ 10 μm, the experimental focal points are found in the vicinity of the rear surface of the ball-lenses (*BFL* < 1μm), see the inset of Fig. 4. In this region, the photonic nanojet effect overwhelms the refractive focusing effect of the ball-lens by dragging the focal point to the ball-lens rear surface. In experiment, the *BFL* < 1 μm is subject of the measurement limit. Eventually, it has been measured as if the back focal plane sits on the rear surface of the sphere.

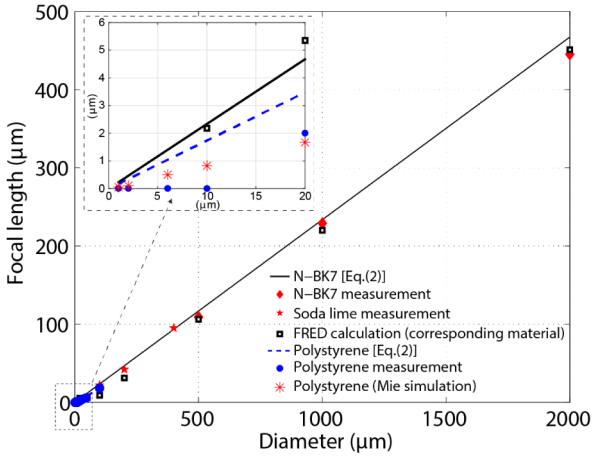

Fig. 4. Focal length *vs* sphere diameter. Lines are calculated data by Eq. (2) and markers are measured data. Open squares of black color are results from the FRED calculation and colored asterisks are from Mie simulation.

5.2 Spot size

We turn our attention to the spot size that was extracted from the same measurements of Fig. 4. Since the spherical aberration shortens focal length, so-called focal shift [20, 21], the NA, which is a ratio between focal length and half aperture size, is difficult to be defined. Moreover, the spherical aberration widens the spot size and causes asymmetry of the spot shape along the optical axis. Due to those effects, it is not a trivial task to derive a simple equation for the spot size of the ball-lens. Therefore, numerical calculations and high-resolution measurements are applied to verify the spot size of the ball-lenses. In Fig. 5, the measured full width at half maximum (FWHM) spot size along the *x*-axis is plotted with

#254854 Received 1 Dec 2015; revised 7 Mar 2016; accepted 8 Mar 2016; published 22 Mar 2016
© 2016 OSA

respect to the diameter of the ball-lens. Similar to the case of the focal length, the ball-lenses smaller than 15 μm (i.e., D ≤ 10 μm) show a particular behavior. The spot size persists to be close to 400 nm independent on the ball-lens diameter. Such a uniform behavior of the spot size is originated from the resolution limit of the measurement system, whose nominal resolution limit is 0.5λ/NA = 357 nm, when the NA = 0.9 objective is employed. However, imperfections of the experimental conditions limit the resolution limit to approximately 400 nm in this case. Nevertheless, it is not expected that this resolution limit significantly affects the conclusion, since the emerging photonic nanojets in theory are expected to lead to a slightly sub-diffraction limited spot size for small spheres (see dark cross markers in Fig. 5, which are the Mie simulation results without the NA filtering). Therefore, even though we reach asymptotically a slightly larger value in the FWHM due to the finite numerical aperture of the system, the conclusion that the measurable FWHM is size independent below a specific diameter will persist. The upper diameter for which this happens is only slightly larger than the one we observe in the experiments, since we are already close to the lower bound of the admissible FWHM. In order to emphasize the photonic nanojet regime, the diameter of the ball-lens is displayed in logarithmic scale in Fig. 5. For the ball-lenses of D ≥ 15 μm, the spot size increases with the diameter. For D < 500 μm, the ray-tracing tools do not produce appropriate results due to the lack of rigorous wave theory. In contrast, for the wavelength-scale spheres, results of the rigorous Mie simulation show a good agreement with experimental results of the spot size, which are plotted with red asterisks in Fig. 5.

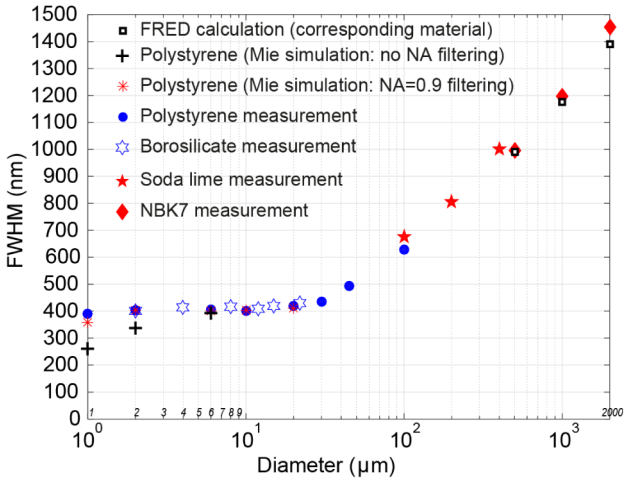

Fig. 5. Measured FWHM spot size in the *x*-axis *vs* sphere diameter. The diameters are displayed in logarithmic scale in order to emphasize the photonic nanojet regime [D ≤ 10 μm].

From the analysis of Figs. 4 and 5, we can identify the photonic nanojet regime as the parameter space where the focal length and the spot size tend to be independent of the ball-lens size, i.e., the back focal plane stays in the vicinity of the rear surface (*BFL* < 1 μm) and the measured FWHM spot size is independent of the ball-lens diameter, which occurs from D ≤ 10 μm in this study.

5.3 Amount of cross-polarization: depolarization effect [14–16]

We can also verify the emergence of the photonic nanojet effect by probing the vector characteristic of the light in the focal plane. In the transverse plane of the vector electric fields, the polarization is divided into parallel and orthogonal field components. In our case, *x*- and *y*-directions, respectively. With the help of an analyzing polarizer, the orthogonal field component (E_y) can be detected by suppressing the parallel field component (E_x). In experiments, a Glan-Taylor polarizer (nominal extinction ratio = 1:10^5) is inserted just after

#254854 Received 1 Dec 2015; revised 7 Mar 2016; accepted 8 Mar 2016; published 22 Mar 2016
© 2016 OSA

the observation objective lens in the HRIM setup. By rotating the analyzer orthogonal to the incident polarization in the x-axis, the E_x can be suppressed to render the amplitude of the E_y component measurable. In experiments, the polystyrene spheres of diameter from 1, 2, 6 and 20 μm are considered. Figure 6 shows the transverse intensity distributions of $E_t = E_x + E_y$ (measured without analyzer) in the upper row and E_y (measured with analyzer) in the lower row. The plotted data are the intensity, which is the square of the field amplitudes

$$I_t = |E_x|^2 + |E_y|^2 \tag{3}$$

$$I_y = |E_y|^2 \tag{4}$$

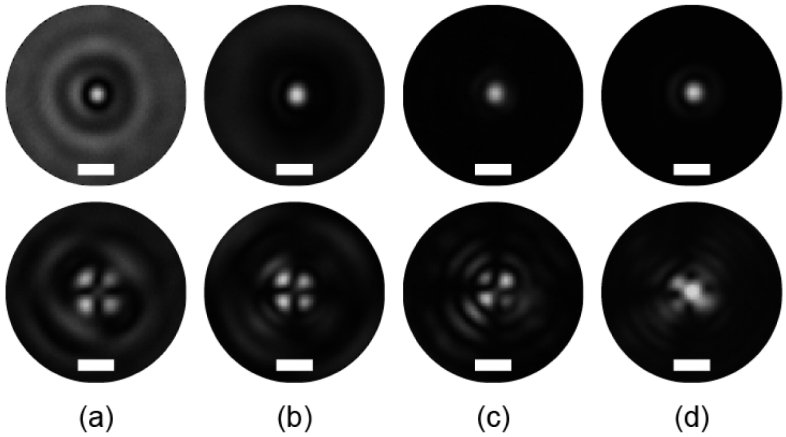

Fig. 6. The measured transverse intensity distributions of the total field components ($E_t = E_x + E_y$) and the orthogonal field component (E_y) in the lower row: (a) D = 1 μm, (b) D = 2 μm, (3) D = 6 μm, and (d) D = 20 μm. The white scale bar indicates 1 μm.

The images are taken in the peak intensity plane along the z-axis. Measurement conditions are set to obtain comparable gray-scale maps of I_t and I_y of each sphere. The four bright spots separated by zero amplitude lines along the x-y axes are the typical feature of the orthogonal field component of focal spots produced by a linearly polarized incidence [15, 16]. This feature is well observed in the lower row of Figs. 6(a)-6(c). Practical extinction ratio of a polarizer is usually limited by imperfection of experimental conditions, such as, alignment and quality of all optical elements. For the 20-μm sphere shown in Fig. 6(d), such experimental errors limit the practical extinction ratio to $1{:}10^3$. When this extinction ratio is taken into account, the Mie simulation reproduces very well the measurement of Fig. 6(d) and shows an excellent agreement, as shown in Fig. 7.

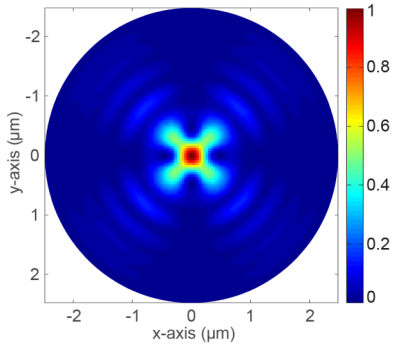

Fig. 7. Reproduced intensity distribution of E_y for the 20-μm sphere shown in Fig. 6(d) using Mie simulation, where the extinction ratio of the polarizer $1{:}10^3$ is taken into account. Intensity is normalized.

#254854 Received 1 Dec 2015; revised 7 Mar 2016; accepted 8 Mar 2016; published 22 Mar 2016
© 2016 OSA

For quantitative investigation, we extract the peak intensity ratio of orthogonal (E_y) and total field (E_t) components from the experiments, and the results are plotted in Fig. 8. Here, practical extinction ratio of a polarizer could be different in each sphere measurement due to imperfect experimental conditions. For the theoretical counterparts, we plot the peak intensity ratio of E_y/E_t from Mie simulation results, which are not subjective to the practical extinction ratio. Larger experimental discrepancy is observed for D = 2 μm and 6 μm cases assumably due to unfavorable experimental conditions. In spite of such a discrepancy, we can clearly see that the amount of the orthogonal field component gets quickly higher for smaller spheres. In this way, we confirm that spheres smaller than 10 μm clearly show a strong vector nature of the fields. In the transition point D ≤ 6 μm, the peak intensity ratio of E_y/E_t becomes larger than $0.5\text{x}10^{-3}$. Beyond this refraction limit, the spheres are operated in the photonic nanojet regime and the cusp catastrophe of the ball-lens vanishes.

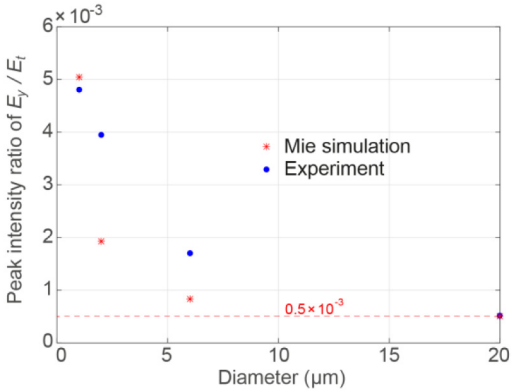

Fig. 8. Peak intensity ratio of E_y/E_t from experiments and Mie simulations.

6. Conclusions

We have studied the refraction limit of the ball-lens, where the cusp catastrophe of imperfect refractive focusing is suppressed by the vector nature of the photonic nanojet effect. In experiments, the existence of the geometrical wavefront has been demonstrated by measuring the phase distributions of the cusp catastrophe, and we observed the disappearance of caustics which are replaced by phase dislocations. In that region, the ray and wave characteristics coexist. In the transitional region, logarithmic-scale intensity maps visualized the vanishing of the cusp catastrophe for the ball-lens diameter D ≤ 10 μm. Three parametric criteria were considered to identify this transitional region as the refraction limit of the ball-lens. First, the focal length shows such a transition as the back focal length becomes close to zero (i.e., the focal plane stays on the vicinity of the rear surface of the ball-lens). Second, the spot size demonstrates that the refraction limit occurs when the FWHM spot size becomes independent of the size of the ball-lenses. Third, the vector nature of light decomposes the field components in parallel and orthogonal ones, in our case, E_x and E_y, respectively. A relatively strong orthogonal component, for instance, a peak intensity ratio of $E_y/E_t > 0.5\text{x}10^{-3}$ for D ≤ 6 μm was confirmed, verifies the emergence of the photonic nanojet effect, where the refraction effect of the spherical aberration is suppressed by the vector character of light and it leads to a tighter confinement. We confirm that wavelength-scale spheres are driven in an operational regime beyond the refraction limit. The aberration effects in the ball-lens focusing start to vanish, and consequently an annihilation of the cusp catastrophe occurs. For glass ball-lenses, the diameter of approximately 10 μm is identified for the refraction limit at λ = 642 nm. Beyond this limit, the refraction of the ball-lens is overwhelmed by diffraction and scattering effects of the photonic nanojet. Note that different material properties could vary the result

#254854 Received 1 Dec 2015; revised 7 Mar 2016; accepted 8 Mar 2016; published 22 Mar 2016
© 2016 OSA

due to dispersion but otherwise the scaling with respect to the wavelength is preserved since Maxwell's equations are scalable.

Acknowledgment

M. F. acknowledges support by the Karlsruhe School of Optics & Photonics (KSOP).

#254854 Received 1 Dec 2015; revised 7 Mar 2016; accepted 8 Mar 2016; published 22 Mar 2016
© 2016 OSA